

PAPER • OPEN ACCESS

Non-axisymmetric MHD simulations of the current quench phase of ITER mitigated disruptions

To cite this article: F.J. Artola *et al* 2022 *Nucl. Fusion* **62** 056023

View the [article online](#) for updates and enhancements.

You may also like

- [Time-dependent runaway electron simulations: Ampere–Faraday equations implemented in CQL3D](#)

R.W. Harvey, Yu.V. Petrov, Charlson C. Kim et al.

- [Plasma profile evolution during disruption mitigation via massive gas injection on MAST](#)

A.J. Thornton, K.J. Gibson, I.T. Chapman et al.

- [Rapid Quenching of Galaxies at Cosmic Noon](#)

Minjung Park, Sirio Belli, Charlie Conroy et al.

Non-axisymmetric MHD simulations of the current quench phase of ITER mitigated disruptions

F.J. Artola^{1,2,*}, A. Loarte², M. Hoelzl¹, M. Lehnen²,
N. Schwarz¹ and the JOEKE Team^a

¹ Max Planck Institute for Plasmaphysics, Boltzmannstr. 2, 85748 Garching, Germany

² ITER Organization, Route de Vinon sur Verdon, 13067 St Paul Lez Durance Cedex, France

E-mail: javier.artola.such@ipp.mpg.de

Received 11 December 2021, revised 8 February 2022

Accepted for publication 16 February 2022

Published 28 March 2022



Abstract

Non-axisymmetric simulations of the current quench phase of ITER disruptions are key to predict asymmetric forces acting into the ITER wall. We present for the first time such simulations for ITER mitigated disruptions at realistic Lundquist numbers. For these strongly mitigated disruptions, we find that the safety factor remains above 2 and the maximal integral horizontal forces remain below 1 MN. The maximal integral vertical force is found to be 13 MN and arises in a time scale given by the resistive wall time as expected from theoretical considerations. In this respect, the vertical force arises after the plasma current has completely decayed, showing the importance of continuing the simulations also in the absence of plasma current. We conclude that the horizontal wall force rotation is not a concern for these strongly mitigated disruptions in ITER, since when the wall forces form, there are no remaining sources of rotation.

Keywords: ITER, disruption, MHD, current quench, forces, mitigated, VDE

(Some figures may appear in colour only in the online journal)

1. Introduction

There is no general consensus on the predictions for the maximum integral wall forces acting on the vacuum vessel during ITER disruptions. Although it is broadly accepted that the maximum total vertical force (F_z) will be of the order of 80 MN [1, 2], the prediction for the horizontal force (F_h) differs at least by an order of magnitude. Using the maximum values found in JET for F_h (~ 4 MN) [3] and extrapolating with Noll's formula [4], maximal horizontal forces of 40 MN are obtained.

* Author to whom any correspondence should be addressed.

^a See Hoelzl *et al* 2021 (<https://doi.org/10.1088/1741-4326/abf99f>) for the JOEKE Team.



Original content from this work may be used under the terms of the [Creative Commons Attribution 4.0 licence](https://creativecommons.org/licenses/by/4.0/). Any further distribution of this work must maintain attribution to the author(s) and the title of the work, journal citation and DOI.

Dedicated studies using a source/sink model inspired by JET measurements [5] also find $F_h \sim 40$ MN [6]. Zakharov's model [7] also recovers a very similar expression to Noll's formula and therefore it also predicts similar forces. However, analytical models based on a 1/1 kink mode that interacts with the vacuum vessel only via eddy currents [8, 9], produce forces at least an order of magnitude smaller. The ratio between the vessel's current decay time (τ_w) and the current quench time (τ_{CQ}) was found to play a major role determining the horizontal force with 3D MHD simulations [10]. In that reference, the maximum force for ITER was $F_h \sim 30$ MN when $\tau_{CQ}/\tau_w \gg 1$ and the minimum force was $F_h \sim 4$ MN when $\tau_{CQ}/\tau_w \ll 1$ (for finite τ_{CQ} and τ_w). Two main effects could be the cause of the strong dependence of the vessel forces with τ_{CQ} . In the following we will refer to the ITER vacuum vessel as 'wall' for simplicity and we define the wall time as $\tau_w \equiv \mu_0 d_w a_w / \eta_w$, where μ_0 is the vacuum permeability and

d_w , a_w and η_w are respectively the thickness, minor radius and resistivity of the wall.

The first effect is related to the evolution of the edge safety factor (q_a). If q_a remains above 2 during a disruption, the 1/1 mode leading to large horizontal forces is not expected. Whether q_a remains above 2 during a disruption depends on the competition between the plasma current decay and the vertical motion of the plasma column (i.e. plasma volume shrinkage). If the vertical motion takes place at constant plasma current (i.e. $\tau_{CQ}/\tau_w \gg 1$), it is expected that q_a decreases below unity [11] and that 1/1 modes become unstable. On the other hand, if the plasma current (I_p) decay is faster than the vertical motion (or decrease of the minor radius ' a '), q_a increases over time since $q_a \propto a^2/I_p$. However, even in the limit where $\tau_{CQ}/\tau_w \ll 1$, elongated plasmas drift vertically in a time scale given by τ_{CQ} [12, 13]. Therefore, the evolution of q_a will be ultimately determined by the function that describes the vertical position as a function of the plasma current ($Z(I_p)$), which is dictated by the geometry of the plasma and the wall in this fast current quench limit.

The second effect arises from the penetration time of the magnetic field across the wall (τ_w). It was derived in [14], that the total wall force can be computed with a surface integral enclosing the wall and plasma volumes

$$\mathbf{F} \equiv \frac{1}{\mu_0} \int_{\text{wall}} \mathbf{J} \times \mathbf{B} dV = \int_{\text{wall}+} \left((\mathbf{B} \cdot \mathbf{n})\mathbf{B} - \frac{B^2}{2}\mathbf{n} \right) dS \quad (1)$$

where $\mathbf{F} \equiv (F_x, F_y, F_z)$, \mathbf{J} is the current density, \mathbf{B} is the total magnetic field and \mathbf{n} is a unit vector perpendicular to the toroidal surface. Therefore, for time scales much shorter than τ_w , the vessel forces remain small ($\mathbf{F} \approx 0$) since \mathbf{B} remains approximately unchanged outside the wall (as observed in [15]). However, as it is deduced from (1) and it is shown in this paper, the force can arise after the field penetrates the wall even in the absence of plasma currents (this was also observed in [16]). Thus, we stress the importance of running these simulations for several τ_w , even when the plasma current has already decayed.

A major finding of our studies is that, in the $\tau_{CQ}/\tau_w \ll 1$ limit, wall forces are static in the toroidal direction (i.e. non-rotating). This is due to the fact that when the wall forces are maximum (when the wall currents decay inside the vacuum vessel) the plasma current has already vanished and thus there is no electromagnetic source to drive the rotation. Therefore the issue of resonances between the force rotation and the natural frequencies of the vacuum vessel [17] is not relevant for this limit. To our knowledge this fact has not been identified in the literature so far.

The mitigation of electromagnetic loads in ITER [18] relies on the dissipation of magnetic energy from the plasma by electromagnetic radiation together with the experimental evidence that the wall forces decrease at smaller τ_{CQ} [19]. Consequently, the ITER disruption mitigation system aims to reduce the plasma temperature during the CQ and thereby τ_{CQ} by using massive material injection. In this paper, we demonstrate with 3D MHD simulations featuring realistic time scales, that

the wall integral forces are indeed largely reduced for mitigated disruptive plasma conditions with respect to the maximal values extrapolated from simple models and empirical assumptions described above.

In section 2, we present the MHD model and in section 3, we present the simulation setup (initial conditions and parameters). Finally, in section 4, we present our results and we summarize our conclusions in section 5.

2. MHD model and assumptions

The basic model employed in this paper is a single temperature visco-resistive MHD model [20]

$$\frac{\partial \mathbf{A}}{\partial t} = \mathbf{v} \times \mathbf{B} - \eta \mathbf{J} - \nabla \Phi, \quad (2)$$

$$\rho \frac{\partial \mathbf{v}}{\partial t} = -\rho \mathbf{v} \cdot \nabla \mathbf{v} - \nabla p + \mathbf{J} \times \mathbf{B} + \nabla \cdot \underline{\underline{\tau}}, \quad (3)$$

$$\frac{\partial \rho}{\partial t} = -\nabla \cdot (\rho \mathbf{v}) + \nabla \cdot (\underline{\underline{D}} \nabla \rho), \quad (4)$$

$$\frac{\partial p}{\partial t} = -\mathbf{v} \cdot \nabla p - \gamma p \nabla \cdot \mathbf{v} + \nabla \cdot (\underline{\underline{\kappa}} \nabla T) \quad (5)$$

that uses the following reduced MHD ansatz for the plasma flow (\mathbf{v}) and the magnetic field (\mathbf{B})

$$\mathbf{B} = \nabla \psi \times \nabla \phi + F_0 \nabla \phi, \quad (6)$$

$$\mathbf{v} = -\frac{R^2}{F_0} \nabla \Phi \times \nabla \phi + \mathbf{v}_{\parallel}, \quad (7)$$

where ψ is the poloidal magnetic flux and $F_0 = RB_\phi$ is taken as a constant in this task. Note that only the poloidal field depends on three spatial coordinates and that the toroidal field only depends on R . Poloidal currents evolve according to current conservation and momentum balance, but we neglect their contribution to the toroidal field [20]. Successful axisymmetric and three-dimensional benchmarks of VDEs have been performed with the full MHD codes NIMROD and M3D-C¹ to check the validity of these assumptions for the wall forces [21, 22]. The quantities shown in equations (2)–(5) are the magnetic vector potential (\mathbf{A}), the ion density (ρ), the total pressure (p), the total temperature ($T \equiv T_e + T_i$), the electrostatic potential (Φ) and the current density (\mathbf{J}). Other parameters in equations (2)–(5) are the plasma resistivity (η), the stress tensor ($\underline{\underline{\tau}}$), the thermal conductivity ($\underline{\underline{\kappa}}$) and the particle diffusion coefficients ($\underline{\underline{D}}$) and the ratio of specific heats (γ). The thermal conductivity coefficient tensor $\underline{\underline{\kappa}}$ presents a high anisotropy (i.e. $\kappa_{\parallel} \gg \kappa_{\perp}$) while the particle diffusion coefficients are normally isotropic.

The equations are numerically solved with the fully implicit JOREK code [20, 23]. Fourier harmonics are used to represent the toroidal direction and for the poloidal plane, third order quadrilateral Bezier finite elements are used (see figure 1). To take into account resistive wall effects, JOREK is implicitly coupled to the STARWALL code [13, 24, 25].

Our modeling for ITER mitigated disruption simulations does not consider either Ohmic heating or radiated power by impurities during the current quench. By neglecting them,

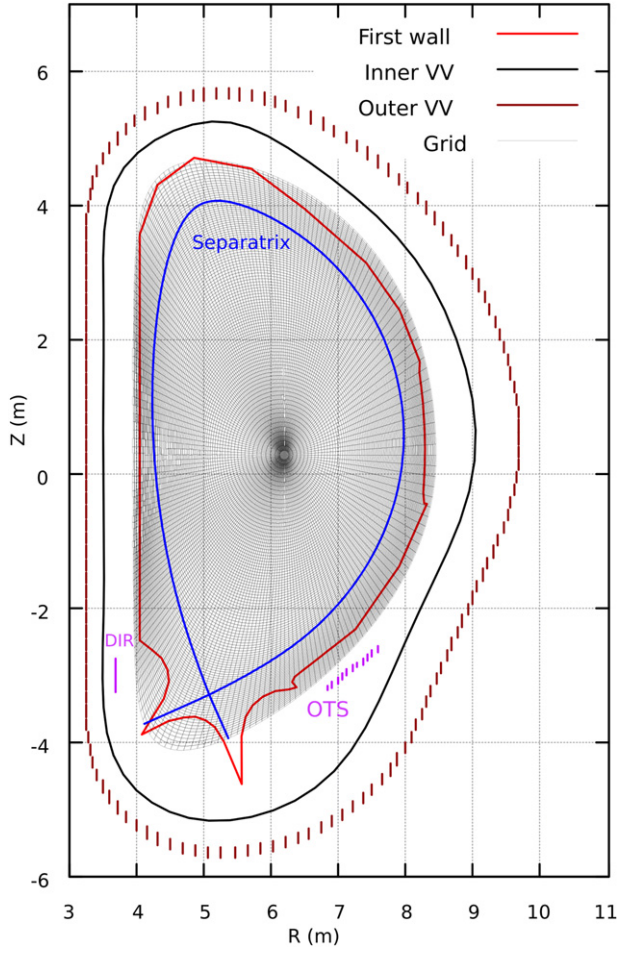


Figure 1. Computational grid and passive components (OTS, DIR, inner and outer vessel) included in our simulations. The ITER first wall (red) and the initial plasma separatrix (blue) are included for reference. Except for the inner vacuum vessel layer, where 3D currents can flow, the current path in the other passive components is toroidal and axisymmetric since they are discretized by set of toroidal filaments.

we assume that their associated terms that should appear in equation (5) exactly cancel each other. In other words, we assume that the plasma magnetic energy is completely radiated. Such an assumption is realistic since radiation efficiencies $>90\%$ are required to mitigate disruptions in ITER DT plasmas [18]. In our case, there are no sources of temperature and density, therefore they are determined by the initial conditions and their evolution through the convection and diffusion/conduction terms.

We model the ITER vacuum vessel composed by inner layer and outer axisymmetric layers using the thin wall approximation (see figure 1). The resistivity and thickness of each layer is given according to the vessel design specifications ($\eta_w = 0.8 \mu\Omega \text{ m}$ and $d_w = 6 \text{ cm}$). Non-axisymmetric currents are allowed to flow in the inner layer, which is discretized with 75 000 thin linear triangles. The outer layer is discretized with toroidal filaments and therefore only axisymmetric toroidal currents flow there. Since we simulate current quench times that are faster than the field penetration time of the inner vessel layer, 3D currents in the outer vessel do not play a role

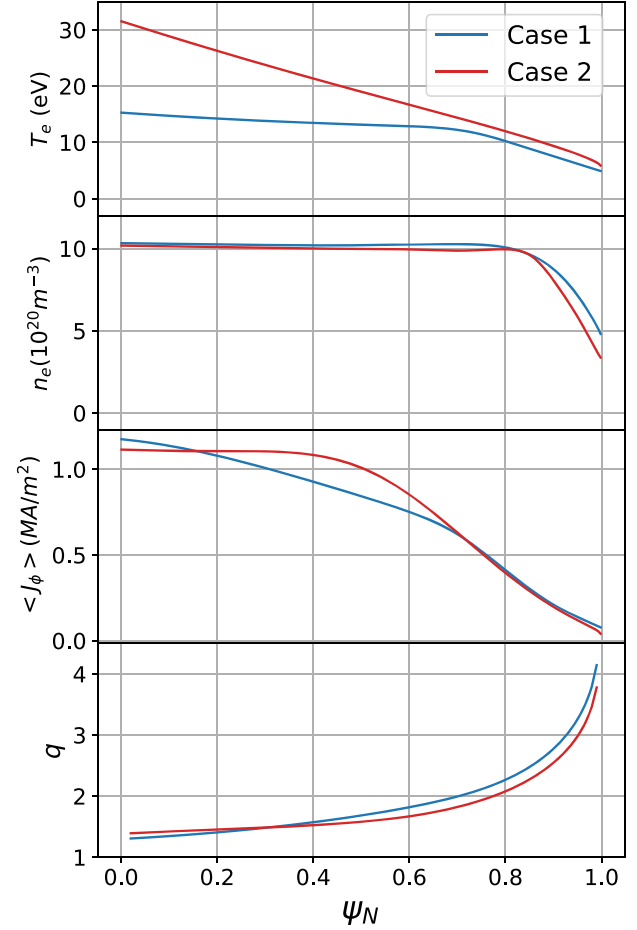


Figure 2. Profiles at the start of the 3D simulations for the two cases considered in this paper. From top to bottom the profiles of the electron temperature, electron density, poloidally averaged toroidal current profile and safety factor profiles are shown. The radial coordinate is the normalized poloidal magnetic flux.

for the plasma dynamics in our case. The outer triangular support (OTS) and the divertor inboard rail (DIR) are also included since they are important passive components for vertical stability. This model for the ITER passive structures has already been benchmarked successfully with the code DINA for axisymmetric simulations [20, 26]. Note that we are not taking into account the ITER blanket modules, which could potentially lead to additional stabilizing effects since dipolar currents with characteristic time scales of $\sim 10 \text{ ms}$ can be induced in these modules. However, toroidal currents cannot circulate directly from module to module since they are insulated from each other and only electrically connected through the vacuum vessel. For these reasons, we do not expect that the presence of blanket modules changes the results presented in this work significantly (i.e. the maximum wall forces).

The computational polar grid (see figure 1) is composed of 100×200 radial and poloidal Bezier elements, respectively. The plasma computational boundary roughly matches the ITER first wall but does not represent the details of the divertor structures adequately. More refined boundaries including sharp edges will be included in future work.

Table 1. Parameters used during the current quench phase. For the temperature dependent parameters the reference temperature is $T_{e0} = 300$ eV. Note that except for η and κ_{\parallel} the coefficients are spatially constant. *Due to numerical problems, μ_{\parallel} had to be increased at some points of the simulation by a factor of 10 (see section 4.4).

Parameter	Value	Description
D	$2 \text{ m}^2 \text{ s}^{-1}$	Isotropic particle diffusion coefficient
κ_{\perp}	$2 \times 10^{21} (\text{m s})^{-1}$	Perpendicular thermal conductivity
$\kappa_{\parallel} = \kappa_0 (T_e/T_{e0})^{5/2}$	$\kappa_0 = 1.77 \times 10^{28} (\text{m s})^{-1}$	Parallel thermal conductivity
$\eta = \eta_0 (T_e/T_{e0})^{-3/2}$	$\eta_0 = 6.74 \times 10^{-7} \Omega \text{m}$	Parallel resistivity
$(\mu_{\parallel}^*, \mu_{\perp})$	$(1630, 4.24) \times 10^{-7} \text{ kg m}^{-1} \text{ s}^{-1}$	Parallel/perpendicular dynamic viscosity

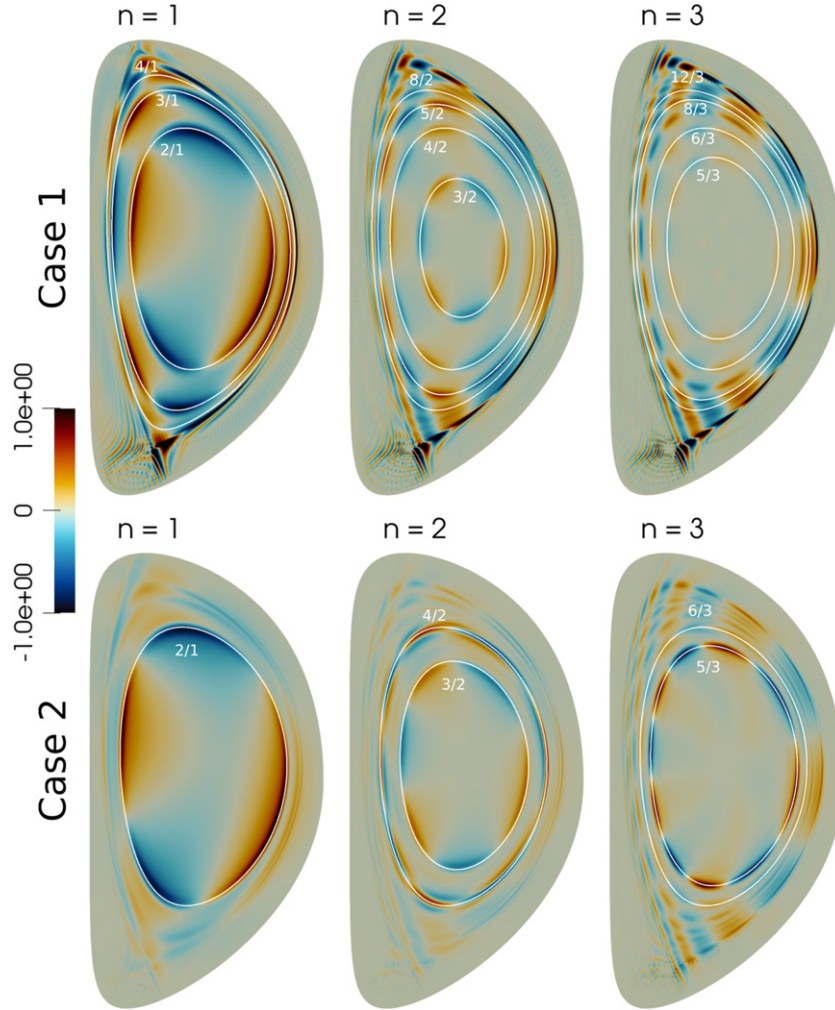


Figure 3. Mode structures of the electric potential (Φ) for case #1 at $t = 8.1$ ms and for case #2 at $t = 4.7$ ms. The white contours represent rational flux surfaces $q = m/n$ which are labeled with their associated poloidal (m) and toroidal (n) mode numbers. The electric potential is normalized to its maximum value for each mode number.

3. Initial conditions and used parameters

The chosen initial conditions correspond to those of a strongly mitigated disruptive plasma in which the thermal quench (TQ) has already taken place. A 15 MA/5.3 T L-mode plasma was considered and the initial conditions were constructed with the following procedure. In the first place, the pre-TQ L-mode reference equilibrium was computed. Secondly, in order to achieve a large electron density, the density profile

was re-scaled by a factor of 20 while the plasma temperature was re-scaled by a factor of 1/20. This procedure allows to keep the pressure profile unchanged and to obtain an identical Grad–Shafranov equilibrium as for the reference L-mode but with higher electron densities and lower temperatures. Finally, the perpendicular thermal transport coefficient (κ_{\perp}) was increased in order to simulate an artificial thermal quench, leading to the profiles shown in figure 2 which are used as starting points for the 3D simulations. By adjusting κ_{\perp} , the two

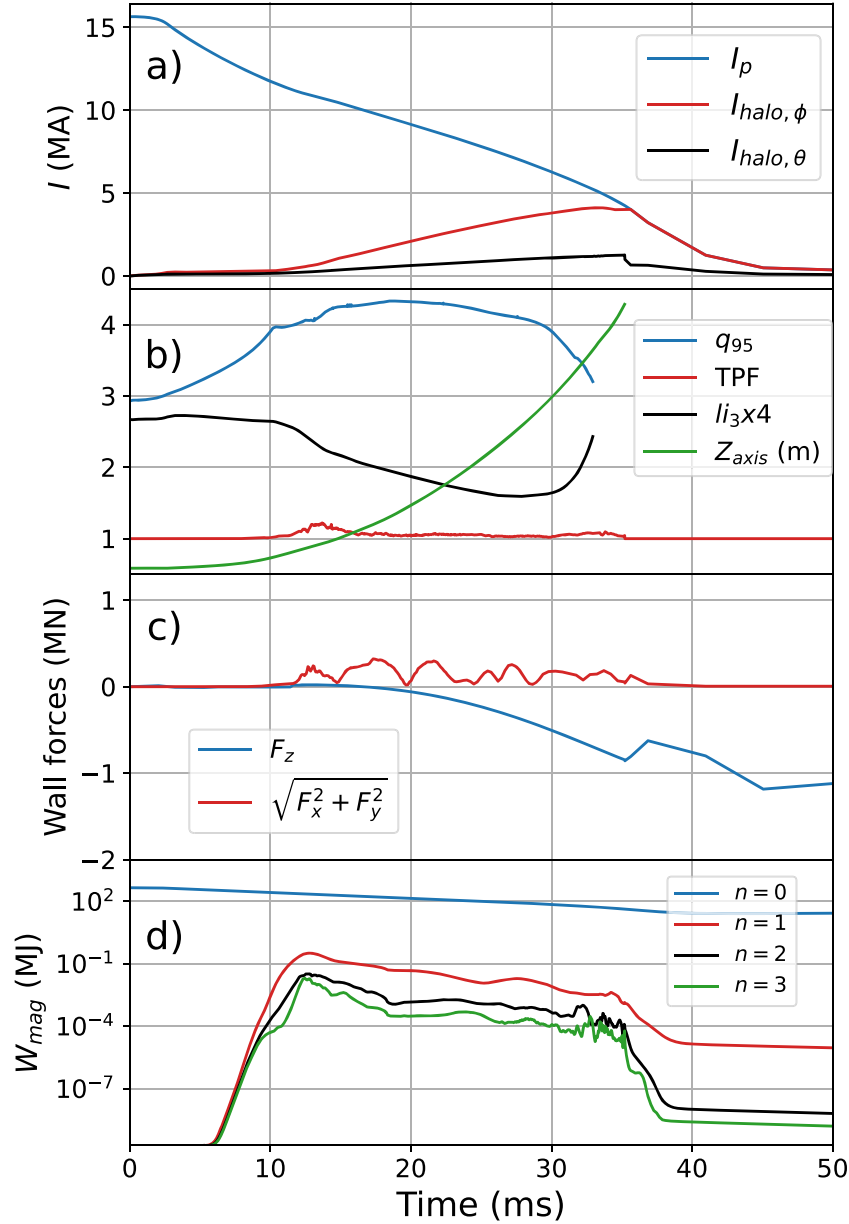


Figure 4. Time traces of the CQ simulation for case #1. (a) Total plasma toroidal current (I_p), total poloidal ($I_{halo,\theta}$) and toroidal ($I_{halo,\phi}$) halo currents. (b) Edge safety factor (q_{95}), toroidal peaking factor of the poloidal halo currents (TPF), internal inductance ($l_i(3)$) and vertical position of the magnetic axis (Z_{axis}). (c) Vertical (F_z) and horizontal wall forces ($\sqrt{F_x^2 + F_y^2}$). (d) The poloidal magnetic energy of the most dominant toroidal mode numbers ($n = 0, 1, 2, 3$).

different cases shown in figure 2 were constructed. These two cases are used to study the sensitivity of the current quench dynamics to differences in the temperature and current density profiles. The resulting temperatures and densities can be expected after the thermal quench following injection of Neon via shattered pellet injection (SPI). Note that the chosen temperatures are close to the Neon radiation peak (~ 30 eV). Once the profiles shown in figure 2 are established, the thermal diffusion coefficients are reduced to avoid a further temperature decay and the 3D simulation of the CQ starts. During the CQ, 11 toroidal Fourier harmonics are considered ranging from 0 to 10 ($n \in [0, 10]$). The plasma parameters used during the current quench phase are listed in table 1.

The safety factor (q) profiles are not completely flattened inside the $q = 2$ surface, which are typically observed to be the relaxed MHD states after the thermal quench [27]. These MHD unstable profiles are chosen intentionally to attain a self-consistent relaxation of the q and J_ϕ profiles during the first phase of the CQ. Rather than starting from arbitrarily stable current density profiles, we consider that in order to obtain a J_ϕ profile similar to the one that would be obtained after a TQ, it is more convenient to start with unstable profiles and allow for a self-consistent relaxation.

We apply Dirichlet boundary conditions for the fluid variables at the plasma–wall interface (ρ , T and \mathbf{v}). The temperature and density boundary conditions are simply

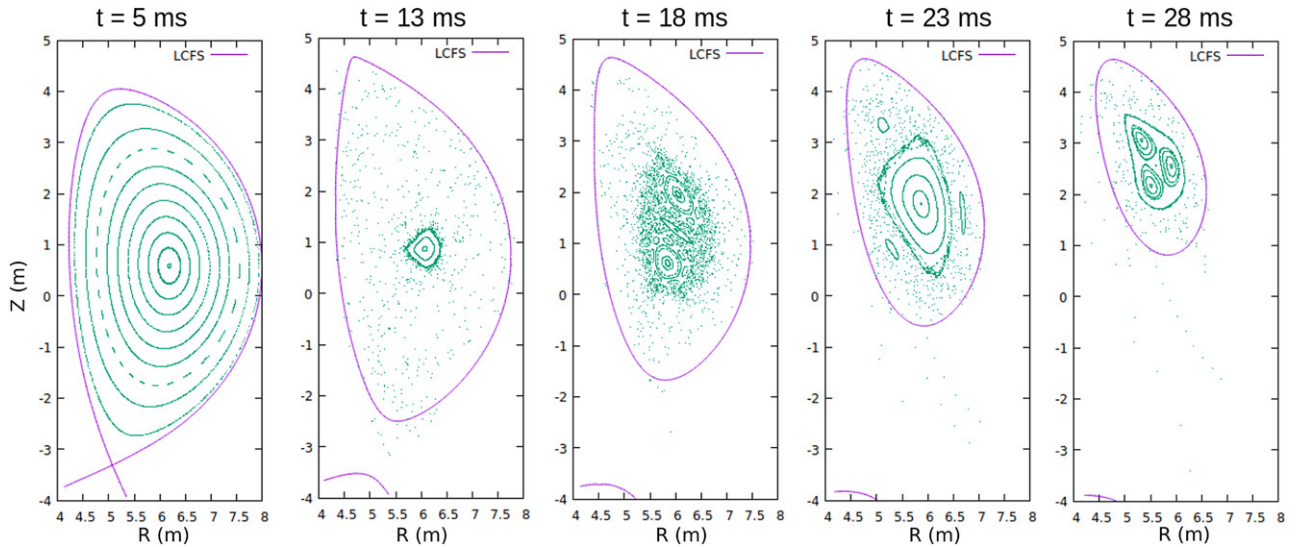


Figure 5. Poincaré plots for case #1. The purple contour represent the LCFS.

$n_e(t) = 10^{20} \text{ m}^{-3}$ and $T_e(t) = 1 \text{ eV}$. In addition we set a no-normal flow boundary condition at the plasma-wall interface ($\mathbf{v} \cdot \mathbf{n} = 0$) and no parallel velocity ($v_{\parallel} = 0$). Note that in our formulation, the $\mathbf{v} \cdot \mathbf{n} = 0$ condition is equivalent of that of an ideal wall in the poloidal direction ($\Phi = 0$). It also implies that energy and particles cannot be lost through the boundary by convection.

4. ITER current quench simulations

In this section we describe and compare the two simulated cases. The main difference between the two cases are the different profiles shown in figure 2, which took $t = 5 \text{ ms}$ and $t = 2.1 \text{ ms}$ to establish for case #1 and #2 by running JOREK axisymmetrically, respectively. Otherwise the employed parameters are the identical (see table 1).

4.1. CQ phase of case #1

For case #1, the axisymmetric run lasted about 5 ms to establish the profiles shown in figure 2. At $t = 5 \text{ ms}$ the 10 non-axisymmetric modes were initialized to ‘noise’ level and the 3D simulation started. The case is unstable to a variety of tearing modes due to the large plasma resistivity and the initial current profile. These modes are linearly unstable, have similar growth rates ($\sim 2\text{--}3 \text{ ms}^{-1}$) and appear at different rational surfaces ($q = m/n$) described by the toroidal (n) and poloidal periodicities (m) as shown in figure 3. The most unstable modes have low- n toroidal mode numbers and the higher- n modes remain subdominant. The evolution of the poloidal magnetic energy for a selection of dominant mode numbers ($n = 1, 2, 3$) is shown in figure 4.

At $t = 10 \text{ ms}$, the modes energies start to saturate and reach their maximum value at $t = 13 \text{ ms}$. Note that at the time of mode saturation, the total plasma current has already decayed to 11–12 MA due to the low plasma temperature. Larger ‘noise’ levels for the initial perturbations could cause the saturation phase to occur at a higher I_p . In this respect, more

realistic initial conditions for the non-axisymmetric modes could be achieved by also simulating the thermal quench, however this is out of the scope of this work. Later on, we will compare this case to case #2, in which, the modes saturate at a higher plasma current (14 MA).

The mode activity causes a slow flattening of the current profile as it can be observed in the evolution of the internal inductance ($l_i(3)$) in figure 4. The MHD modes lead to the destruction of a significant fraction of the magnetic flux surfaces as shown in the Poincaré plots of figure 5. Almost complete ergodization of the field line topology is found at $t = 13 \text{ ms}$ while at $t = 23 \text{ ms}$ flux-surfaces reappear at the plasma core. The confinement of runaway electrons in the 3D perturbed fields produced with this simulation is studied in [28], showing that they will be quickly depleted at $t = 13 \text{ ms}$ but that they could re-appear in the re-formed core flux surfaces ($t = 23 \text{ ms}$).

As I_p decays, the plasma moves vertically upwards and toroidal current in the halo region is induced (see I_p , Z_{axis} and $I_{\text{halo},\phi}$ traces in figure 4). The CQ time defined as $\tau_{\text{CQ}} \equiv (t_{20\%} - t_{80\%})/0.6$ [29] is 47 ms, which is close to the envisaged minimum CQ time for mitigated disruptions (50 ms) [1]. Such evolution leads to an edge safety factor (q_{95} trace) that remains in a range of 3–4. The effects of the halo currents in the evolution of q_{95} will be discussed in section 4.4.

Since q_{95} stays above the value of 3, modes that could result in large horizontal wall forces are not observed (i.e. $m/n = 1/1$ modes). Accordingly, the horizontal force remains at the noise level (see $\sqrt{F_x^2 + F_y^2}$ trace in figure 4). The maximum toroidal peaking factor of the poloidal halo currents (TPF trace in figure 4) is 1.2 and arises when the halo current fraction (HF) is still very small (2%). We define the halo fraction as the total poloidal halo current ($I_{\text{halo},\theta}$) normalized by the pre-disruptive toroidal plasma current (as defined in [10]). The TPF is

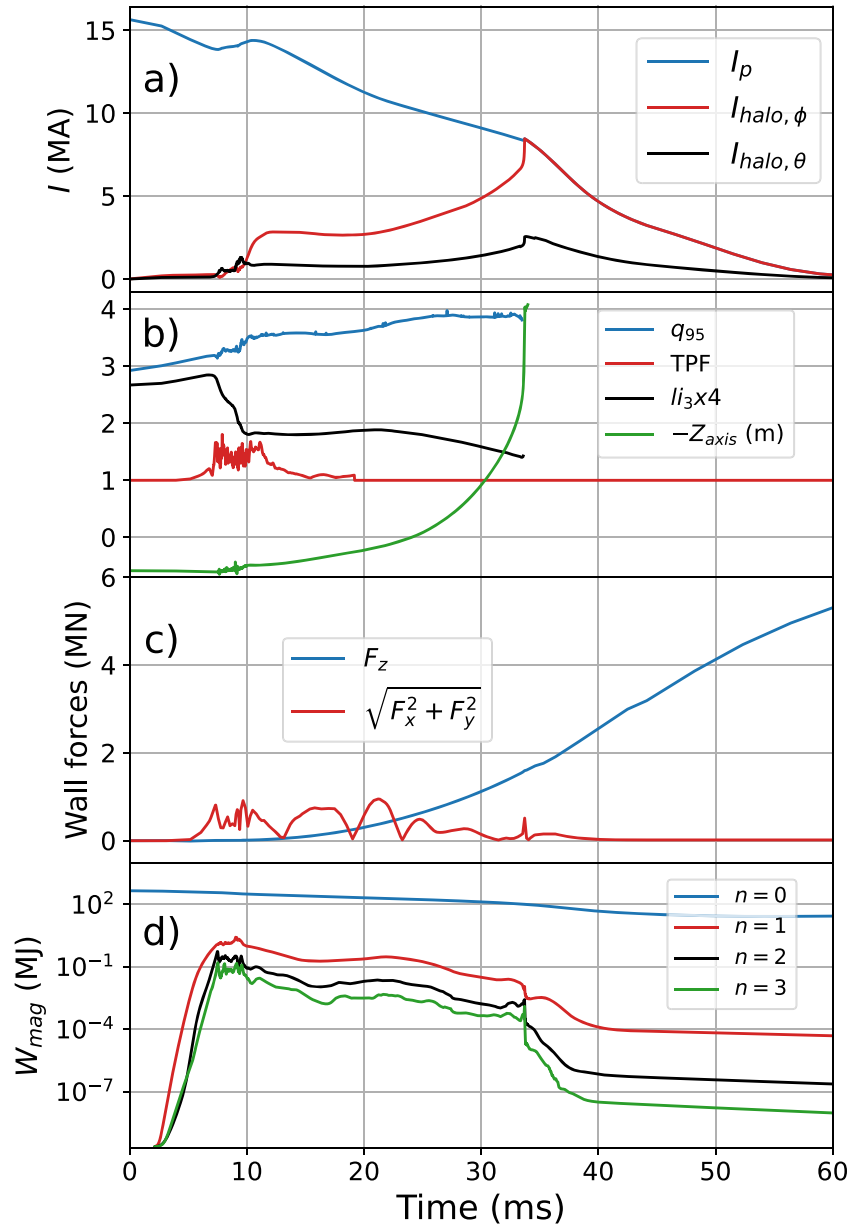


Figure 6. Time traces of the CQ simulation for case #2. (a) Total plasma toroidal current (I_p), total poloidal ($I_{halo,\theta}$) and toroidal ($I_{halo,\phi}$) halo currents. (b) Edge safety factor (q_{95}), toroidal peaking factor of the poloidal halo currents (TPF), internal inductance ($l_i(3)$) and vertical position of the magnetic axis (Z_{axis}). (c) Vertical (F_z) and horizontal wall forces ($\sqrt{F_x^2 + F_y^2}$). (d) The poloidal magnetic energy of the most dominant toroidal mode numbers ($n = 0, 1, 2, 3$).

defined as

$$TPF \equiv \max \left(\frac{1}{2} \oint_{\phi} |\mathbf{J} \cdot \mathbf{n}| R d\ell \right) / (I_{halo,\theta} / 2\pi) \quad (8)$$

where $\mathbf{J} \cdot \mathbf{n}$ is the normal current density into the wall and $d\ell$ is the differential poloidal length of the wall's contour at a given ϕ . The maximum value of the $HF \times TPF$ product is 0.09, which is significantly lower than the largest products of 0.75 observed in current experiments [29] as it is expected for mitigated disruptions. A value of the $HF \times TPF$ product below 0.15 corresponds to category I (frequent occurrence) electromagnetic transients considered for the ITER design [18]. The toroidal

halo current shown in figures 4 and 6 is the total toroidal current in the open field line region, which is delimited by the first wall and by the last closed flux surface (LCFS) calculated from the $n = 0$ component of ψ .

4.2. CQ phase of case #2

For case #2, the axisymmetric run lasted about 2.1 ms to establish the profiles shown in figure 2 and the non-axisymmetric modes were initialized to noise level at that point in time. Similar to case #1, several tearing modes are unstable as shown in figure 3 but here a stronger dominance of the 2/1 mode is observed. The evolution of the magnetic energy for a selection of dominant mode numbers ($n = 1, 2, 3$) is shown in figure 6.

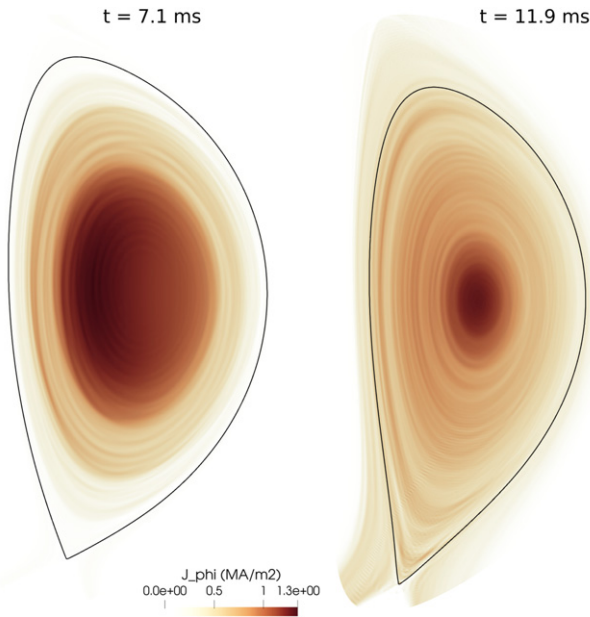


Figure 7. 2D distribution of the toroidal current density of the $n = 0$ mode for case #2 at $t = 7.1$ ms and $t = 11.9$ ms. The black contour corresponds to the LCFS. The figure shows how the current density profile flattens beyond the LCFS.

Contrary to case #1, the saturation of the modes energy takes place at a larger fraction of the initial plasma current ($I_p \approx 14$ MA at $t = 7$ ms). The non-linear growth of non-axisymmetric modes causes a large and quick flattening of the current profile as indicated by the $l_i(3)$ trace in figure 6. It is noteworthy that the large drop in inductance ($\Delta l_i(3) = 0.26$ in 3.3 ms) is followed by an increase of the current in the halo region and a spike in the total current. This suggests that the current flattening caused by the MHD activity takes place also beyond the LCFS, and that scrape-off layer currents may be playing a important role when describing the typical I_p -spikes that are routinely observed in disruptive plasmas. The distributions of the current and temperature before and after the flattening caused by the MHD activity are presented in figures 7 and 8 respectively.

The resulting current quench time for this simulation is $\tau_{CQ} = 45.5$ ms, which is also close to the minimum allowed by ITER specifications (50 ms). In contrast with case #1, the plasma drifts vertically downwards as I_p decays (note the minus sign in front of the Z_{axis} trace in figure 6). We attribute this change of direction to the stronger drop in $l_i(3)$ for case #2. It was found in [30] that large drops of the internal inductance during major disruptions in ITER lead to downward displacements. Similarly for the ASDEX-Upgrade tokamak [31], it was found that drops of l_i in lower single-null plasmas cause a ‘vertical dragging effect’ that moves the plasma downwards.

Similar to case #1, q_{95} remains in the range of 3–4 during the CQ and the horizontal force remains at noise level (below 1 MN). The maximum TPF is 1.7 and arises when the halo fraction is 5.7%. The maximum $HF \times TPF$ product is 0.17 which is two times larger than in case #1. This is still far from the largest experimental products (0.75), but slightly above the level for category I electromagnetic transients in ITER (0.15).

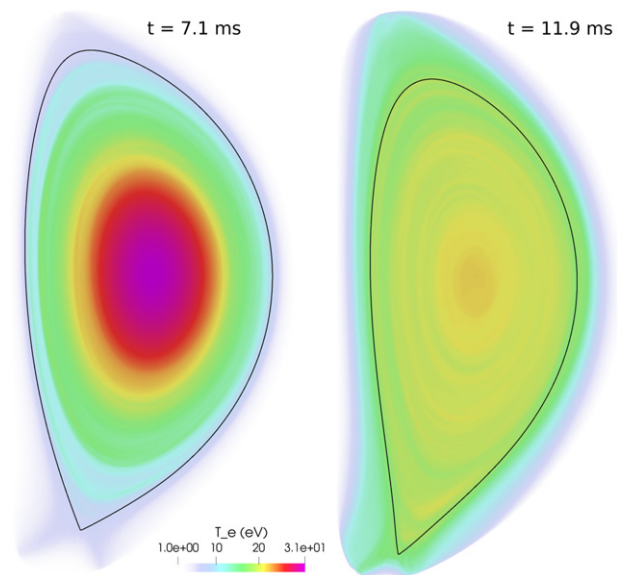


Figure 8. 2D distribution of the electron temperature of the $n = 0$ mode for case #2 at $t = 7.1$ ms and $t = 11.9$ ms. The black contour corresponds to the LCFS. The figure shows how the temperature profile flattens beyond the LCFS.

4.3. Wall forces after the current quench

We continue the simulation after the plasma current has completely decayed. During that phase, induced wall currents during the CQ relax and decay, leading to the penetration of the magnetic field across the wall and to the rise of net wall forces. As seen in figure 9, the vertical force arises in a time scale given by the L/R time of the vacuum vessel ($\tau_w \sim 500$ ms). The wall time (τ_w) is about two times larger than in [2, 10] due to the fact that only a single vacuum vessel layer was considered in those references instead of the two layers that must be taken into account to represent ITER structures. Note that the time traces of the vertical forces are very similar to the ones obtained in [32] for ITER disruptions with volumetric walls. Both cases show similar vertical maximal forces in the range of 11–14 MN despite the different directions for the vertical displacement. At the time of maximal vertical force, the distribution of the current density in the inner vacuum vessel is roughly identical (see figure 10). In addition, we checked that the current distribution in the other passive components are also similar for both cases. Since the wall force and the final current distribution is independent of the vertical motion direction, we conclude that the vertical force arises due to the distribution of the net toroidal wall current along the wall contour and its interaction with the magnetic field produced by the poloidal field coils. Such force would in principle not arise in the case of a fully up-down symmetric plasma centered in an up-down symmetric wall before the CQ starts, which points to the advantage of having up/down symmetric plasmas and reactor designs to minimize disruption forces. However as depicted in figure 1, the plasma and wall structures are not up-down symmetric in ITER and therefore, it is natural that these asymmetries lead to net wall forces due to a net toroidal current. In any case, the

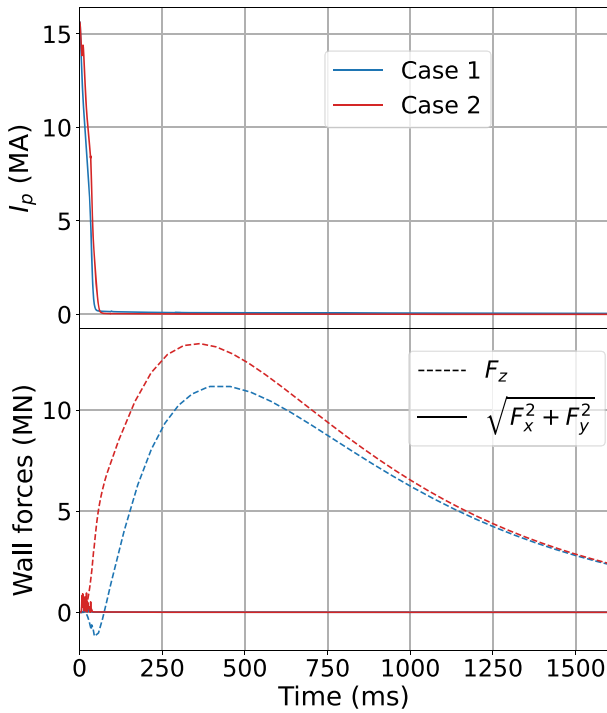


Figure 9. Total plasma current and wall forces for the simulated cases. Case #1 and #2 are shown in blue and red respectively. In the bottom plot, the vertical force (dashed) and the horizontal force (solid) are shown.

magnitude of the maximum F_z is a factor 6 smaller than the largest estimates [1]. Finally the horizontal force completely decays at the moment the plasma current vanishes, confirming that the found horizontal force is noise arising from a finite employed resolution.

4.4. Influence of halo currents and other parameters

In our model the temperature at the plasma–wall interface is initialized with an electron temperature of 1 eV. As the plasma is scraped-off due to the vertical motion and as the ergodic field lines connect the plasma core with the halo region, the SOL temperature increases. As shown in figure 8, the temperature can reach values of 10–15 eV in this region during the CQ. Such temperatures are consistent with experimental temperature measurements at the plasma–wall interface during disruptions [33]. At these temperatures, the Spitzer–Harm parallel conductivity ($\kappa_{\parallel} \propto T_e^{2.5}$) remains moderate and allows significant temperatures/temperature gradients in the SOL to carry the corresponding heat-flux. Estimates for ITER field line lengths of 100 m at $T_e = 10$ eV and $n_e = 10^{20} \text{ m}^{-3}$ give characteristic parallel conduction times of the order of 70 ms.

Parallel convection was found not to be sufficient to decrease the SOL temperature to lower values, although we could not run the case at lower parallel viscosities due to the appearance of numerical instabilities in the v_{\parallel} variable. In addition, the parallel viscosity had to be increased by an extra factor of 10 at some points of the simulations to deal with such numerical problems (specifically at $t = 14.3$ ms for case #1 and at $t = 19.8$ ms for case #2). However, when

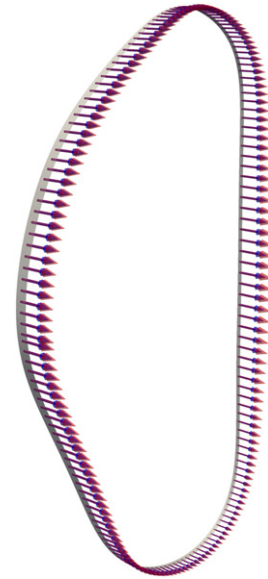


Figure 10. Current density distribution in the inner vessel at $\phi = 0$ when the vertical force is maximum ($t = 420$ ms for case #1 and $t = 360$ for case #2). The blue and red arrows represent the current density magnitude of case #1 and case #2 respectively.

comparing re-run fragments of the simulation with and without the increase of μ_{\parallel} we did not observe a significant difference in the evolution of q_{95} , the magnetic energies or the wall forces. Note here that convection can transport thermal energy toward the plasma–wall interface, but this energy can only be lost there by conduction since we set a no-normal flow condition ($\mathbf{v} \cdot \mathbf{n} = 0$).

We note that stronger energy sinks in the halo region could decrease the temperature and consequently the total halo currents. In principle, the total halo currents can change the evolution of q_{95} . When the halo current flow is limited to very low values due to very low temperatures in the halo, the current that otherwise would be induced in the halo can be partially re-induced in the core, thus slowing down the I_p decay with respect to the vertical motion and leading to smaller q_{95} values that can potentially drive larger asymmetries in the halo currents. The maximal toroidal halo currents found here (4.1 MA for case #1 and 8.4 MA for case #2) and the maximal poloidal halo current fractions (8.7% for case #1 and 16.6% for case #2) are within (or very close for case #2) to the ITER specifications for category I electromagnetic transients.

More advanced SOL models including Ohmic heating, impurity transport and radiation, neutral particles and sheath boundary conditions are needed to reliably predict the temperatures and densities in the halo region and thus the correct evolution of q_{95} . In future works we will pursue such simulations.

5. Conclusions

We have presented non-axisymmetric MHD simulations of the current quench phase of ITER mitigated plasmas in a comprehensive manner. The chosen parameters include realistic Lundquist numbers (or Spitzer resistivities) and parallel heat

conductivity. Due to the high computational cost of such simulations (of the order of 5 million core.hours per simulation) we present two cases featuring an upwards and a downwards vertical displacement. Additional scans will be performed in further follow-up studies.

Both cases show that the integral wall forces will be highly reduced for mitigated plasmas with respect to the largest expected values. We find horizontal forces below 1 MN, with the largest extrapolations from JET being ~ 40 MN when using Noll's formula. We attribute the absence of the horizontal forces to the lack of 1/1 modes as q_{95} remains above the value of 3 during the current quench. Such beneficial evolution of q_{95} originates from the fast current quench time (~ 50 ms) compared to the wall current decay time (~ 500 ms) and the induced toroidal halo currents. Further analysis including more advanced models of the halo region and scans on τ_{CQ} will be pursued in future studies. Apart from more refined models of the SOL, we will also pursue studies including the toroidal asymmetries of the ITER vacuum vessel that have not been taken into account in this work. The vessel asymmetries need further assessment since they can potentially impact the current flow and thus the asymmetries of forces during ITER disruptions.

A maximum vertical force of 11–14 MN is found regardless of the direction of the plasma vertical motion. Such force is attributed to the diffusion of the net wall current in an up-down asymmetric vessel and its interaction with the poloidal field coils. The simulated mitigated disruptions show a reduction of the vertical force by a factor of 6 with respect to the largest expected values (80 MN), which confirms the effectiveness of the ITER mitigation strategy and that halo currents are within the category I boundary. For disruptions with CQ times much shorter than the wall's resistive time, our simulations also point to the fact that disruption forces can be minimized if the pre-TQ plasma and vessel structures are up/down symmetric, which has implications for DEMO reactor designs.

We also highlight the potential importance of considering the SOL to describe the I_p -spike phenomenon that is typically observed in tokamak disruptions [34]. As it has been shown in this work, the flattening of the toroidal current and temperature profiles due to the MHD activity takes place beyond the LCFS.

Finally we conclude that the horizontal wall force rotation is not a concern for these highly mitigated plasma disruptions in ITER, since when the wall forces form, there are no remaining sources of rotation (i.e. the plasma current has decayed already).

Acknowledgments

ITER is the Nuclear Facility INB No. 174. This paper explores physics processes during the plasma operation of the tokamak when disruptions take place; nevertheless the nuclear operator is not constrained by the results presented here. The views and opinions expressed herein do not necessarily reflect those of the ITER Organization. The simulations presented here have been performed using the ITER HPC cluster, the Marconi-Fusion supercomputer and Google Cloud resources

provided to the ITER Organization under the Cloud computing proof of concept collaboration. We would like to thank S. Pinches, Frederic Hamiez and Peter Kroul for their technical assistance with these simulations. This work has been carried out within the framework of the EUROfusion Consortium and has received funding from the Euratom Research and Training Program 2014–2018 and 2019–2020 under Grant Agreement No. 633053. The views and opinions expressed herein do not necessarily reflect those of the European Commission.

ORCID iDs

F.J. Artola  <https://orcid.org/0000-0001-7962-1093>
 A. Loarte  <https://orcid.org/0000-0001-9592-1117>
 M. Hoelzl  <https://orcid.org/0000-0001-7921-9176>
 M. Lehnen  <https://orcid.org/0000-0001-6043-8803>
 N. Schwarz  <https://orcid.org/0000-0002-0574-1233>

References

- [1] Sugihara M., Shimada M., Fujieda H., Gribov Y., Ioki K., Kawano Y., Khayrutdinov R., Lukash V. and Ohmori J. 2007 Disruption scenarios, their mitigation and operation window in ITER *Nucl. Fusion* **47** 337–52
- [2] Clauser C.F., Jardin S.C. and Ferraro N.M. 2019 Vertical forces during vertical displacement events in an ITER plasma and the role of halo currents *Nucl. Fusion* **59** 126037
- [3] Gerasimov S.N. et al 2015 JET and COMPASS asymmetrical disruptions *Nucl. Fusion* **55** 113006
- [4] Noll P., Andrew P., Buzio M., Litunovsky R., Raimondi T., Riccardo V. and Verrecchia M. 1997 Present understanding of electromagnetic behaviour during disruptions in JET *Fusion Technology* 1996 ed C. Varandas and F. Serra (Oxford: Elsevier) pp 751–4
- [5] Riccardo V., Noll P. and Walker S.P. 2000 Forces between plasma, vessel and TF coils during AVDEs at JET *Nucl. Fusion* **40** 1805–10
- [6] Bachmann C. et al 2011 Specification of asymmetric VDE loads of the ITER tokamak *Fusion Eng. Des.* **86** 1915–9
- [7] Zakharov L.E., Galkin S.A. and Gerasimov S.N. (JET-EFDA contributors) 2012 Understanding disruptions in tokamaks *Phys. Plasmas* **19** 055703
- [8] Pustovitov V.D., Rubinacci G. and Villone F. 2021 Sideways force due to coupled rotating kink modes in tokamaks *Nucl. Fusion* **61** 036018
- [9] Mironov D.V. and Pustovitov V.D. 2017 Sideways force due to coupled kink modes in tokamaks *Phys. Plasmas* **24** 092508
- [10] Strauss H. 2018 Reduction of asymmetric wall force in ITER disruptions with fast current quench *Phys. Plasmas* **25** 020702
- [11] Artola F.J., Lackner K., Huijsmans G.T.A., Hoelzl M., Nardon E. and Loarte A. 2020 Understanding the reduction of the edge safety factor during hot VDEs and fast edge cooling events *Phys. Plasmas* **27** 032501
- [12] Kiramov D.I. and Breizman B.N. 2017 Model of vertical plasma motion during the current quench *Phys. Plasmas* **24** 100702
- [13] Artola Such F.J. 2018 Free-boundary simulations of MHD plasma instabilities in tokamaks *Theses Université Aix Marseille* (available from: <https://tel.archives-ouvertes.fr/tel-02012234>)
- [14] Pustovitov V.D. 2015 General approach to the problem of disruption forces in tokamaks *Nucl. Fusion* **55** 113032

- [15] Pustovitov V.D., Rubinacci G. and Villone F. 2017 On the computation of the disruption forces in tokamaks *Nucl. Fusion* **57** 126038
- [16] Yanovskiy V.V. *et al* 2021 Global forces on the COMPASS-U wall during plasma disruptions *Nucl. Fusion* **61** 096016
- [17] Schioler T., Bachmann C., Mazzone G. and Sannazzaro G. 2011 Dynamic response of the ITER tokamak during asymmetric VDEs *Fusion Eng. Des.* **86** 1963–6
- [18] Lehnen M. *et al* 2015 Disruptions in ITER and strategies for their control and mitigation *J. Nucl. Mater.* **463** 39–48
- [19] Pautasso G. *et al* 2016 Disruption mitigation by injection of small quantities of noble gas in ASDEX Upgrade *Plasma Phys. Control. Fusion* **59** 014046
- [20] Hoelzl M. *et al* 2021 The JOREK non-linear extended MHD code and applications to large-scale instabilities and their control in magnetically confined fusion plasmas *Nucl. Fusion* **61** 065001
- [21] Krebs I., Artola F.J., Sovinec C.R., Jardin S.C., Bunkers K.J., Hoelzl M. and Ferraro N.M. 2020 Axisymmetric simulations of vertical displacement events in tokamaks: a benchmark of M3D-C1, NIMROD, and JOREK *Phys. Plasmas* **27** 022505
- [22] Artola F.J., Sovinec C.R., Jardin S.C., Hoelzl M., Krebs I. and Clauser C. 2021 3D simulations of vertical displacement events in tokamaks: a benchmark of M3D-C1, NIMROD, and JOREK *Phys. Plasmas* **28** 052511
- [23] Huysmans G.T.A. and Czarny O. 2007 MHD stability in X-point geometry: simulation of ELMs *Nucl. Fusion* **47** 659–66
- [24] Merkel P. and Strumberger E. 2015 Linear MHD stability studies with the STARWALL code (arXiv:1508.04911)
- [25] Hölzl M., Merkel P., Huysmans G.T.A., Nardon E., Strumberger E., McAdams R., Chapman I., Günter S. and Lackner K. 2012 Coupling JOREK and STARWALL codes for non-linear resistive-wall simulations *J. Phys.: Conf. Ser.* **401** 012010
- [26] Artola F.J., Huysmans G.T.A., Hoelzl M., Beyer P., Loarte A. and Gribov Y. 2018 Non-linear magnetohydrodynamic simulations of edge localised mode triggering via vertical position oscillations in ITER *Nucl. Fusion* **58** 096018
- [27] Nardon E. *et al* 2021 Thermal quench and current profile relaxation dynamics in massive-material-injection-triggered tokamak disruptions *Plasma Phys. Control. Fusion* **63** 115006
- [28] Särkimäki K., Artola F.J. and Hoelzl M. 2021 Confinement of passing and trapped runaway electrons in simulation of ITER current quench private communication
- [29] Eidietis N.W. *et al* 2015 The ITPA disruption database *Nucl. Fusion* **55** 063030
- [30] Lukash V., Sugihara M., Gribov Y. and Fujieda H. 2005 Analysis of the direction of plasma vertical movement during major disruptions in ITER *Plasma Phys. Control. Fusion* **47** 2077–86
- [31] Nakamura Y., Yoshino R., Pomphrey N. and Jardin S.C. 1996 Acceleration mechanism of vertical displacement event and its amelioration in tokamak disruptions *J. Nucl. Sci. Technol.* **33** 609–19
- [32] Albanese R. *et al* 2015 Effects of asymmetric vertical disruptions on ITER components *Fusion Eng. Des.* **94** 7–21
- [33] Artola F.J. *et al* 2021 Simulations of COMPASS vertical displacement events with a self-consistent model for halo currents including neutrals and sheath boundary conditions *Plasma Phys. Control. Fusion* **63** 064004
- [34] Wesson J.A., Ward D.J. and Rosenbluth M.N. 1990 Negative voltage spike in tokamak disruptions *Nucl. Fusion* **30** 1011–4